The closure of a shallow tidal inlet promoted by infragravity waves

Xavier Bertin[1], Diogo Mendes[2,3,4], Kévin Martins[1,5], André B. Fortunato[3], Laura Lavaud[1]

[1]UMR 7266 LIENSs CNRS-La Rochelle Université, 2 rue Olympe de Gouges, 17000 La Rochelle, France
[2]CERIS, Instituto Superior Técnico, Universidade de Lisboa, Lisbon, Portugal
[3]National Laboratory for Civil Engineering, Av. do Brasil, 101, 1700-066 Lisbon, Portugal
[4]Hydrographic Institute, Rua das Trinas, 49, 1200-677 Lisbon, Portugal
[5]now at UMR 5805 EPOC CNRS-Université de Bordeaux, Allée Geoffroy Saint-Hilaire, F-33615 Pessac, France

Key Points:

- Under storm waves, infragravity waves up to 0.4 m-high propagate through a shallow inlet at flood but are blocked at ebb.
- At the passage of an infragravity wave crest, currents peak over 2.5 $m.s^{-1}$ and sand fluxes increase by two orders of magnitude.
- Over a tidal cycle, large amounts of sand accumulate at the lagoon entrance, which damps tidal propagation and promotes inlet closure.

Corresponding author: Xavier Bertin, `xbertin@univ-lr.fr`

Abstract

Tidal inlets connect the ocean to inner water bodies and are present worldwide. Shallow inlets display fast morphological changes, due to complex interactions between tides, waves and shallow depths. Their closure is commonly observed under storm waves, but the underlying processes remain only partly understood. Here, we present new field evidence that infragravity waves contribute to the closure of shallow inlets. The analysis of new field data collected at a shallow inlet under storm waves reveals that infragravity waves up to 0.4 m-high can propagate inside the lagoon during flood, but are blocked by opposing currents during ebb. At the passage of an infragravity wave crest, currents peak over $2.5\,\mathrm{m.s^{-1}}$ and increase instantaneous sand fluxes by two orders of magnitude. Large accumulations of sand at the lagoon entrance damp tidal propagation until full inlet closure. This mechanism provides a new explanation for the closure of shallow inlets observed worldwide.

1 Introduction

Tidal inlets connect the ocean to inner water bodies and concentrate socio-economic and environmental challenges, such as the maintenance of navigation routes and water quality, the mitigation of flooding risk in the backbarrier lagoons and the stabilization of often urbanized adjacent shorelines. Small tidal inlets are particularly dynamic coastal systems, due to the combination of tides, waves and the presence of shallow channels and sandbanks. These dynamics are still only partly understood and drive fast and large morphological changes, making tidal inlet behaviour hard to predict. Tidal inlets will also be substantially impacted by ongoing climate changes [*Duong et al.*, 2016], so that their sustainable management constitutes a major challenge worldwide. Among the fast morphological changes that these coastal systems exhibit, the closure of intermittent inlets is commonly observed in many regions of the world [*McSweeney et al.*, 2017], such as Southwest Europe [*Moreno et al.*, 2010; *Fortunato et al.*, 2014; *González-Villanueva et al.*, 2017], North America [*Hanes et al.*, 2011; *Orescanin and Scooler*, 2018], West [*Anthony et al.*, 2002] and South Africa [*Cooper*, 2001] and Australia [*Ranasinghe and Pattiaratchi*, 2003]. Yet, the underlying processes are still not totally understood while process-based numerical models usually fail to reproduce this behaviour [e.g. *Bertin et al.*, 2009].

Williams and Stacey [2016] performed field measurements at a shallow inlet in Northern California and identified fluctuations in water levels and current velocities with periods of the order of the minute. These fluctuations were interpreted as infragravity waves (hereafter referred to as IG waves), which correspond to long waves associated with the presence of groups in incident short waves [see *Bertin et al.*, 2018, for a recent review]. These authors also showed that velocities associated with IG waves were of the same order of magnitude or even larger than tidal currents, although they rapidly decreased after the beginning of the ebb. *Bertin and Olabarrieta* [2016] combined field observations and numerical modelling at the Albufeira Lagoon Inlet (SW Portugal, Fig. 1-A) and revealed the occurrence of similar oscillations in water levels and current velocities in the IG frequency band. While these fluctuations were present over the ebb-tidal delta during the whole tidal cycle, they only appeared between the beginning of the flood and up to two hours after high tide inside the lagoon. This behavior was explained by IG wave blocking due to strong counter tidal currents in shallow water depths. *Bertin and Olabarrieta* [2016] proposed that the occurrence of these fluctuations mostly during flood and not during ebb could promote flood dominance in the lagoon and possibly contribute to their closure during storms. The present study aims at verifying this hypothesis, based on an unpublished field dataset collected at the Albufeira Lagoon Inlet under storm waves.
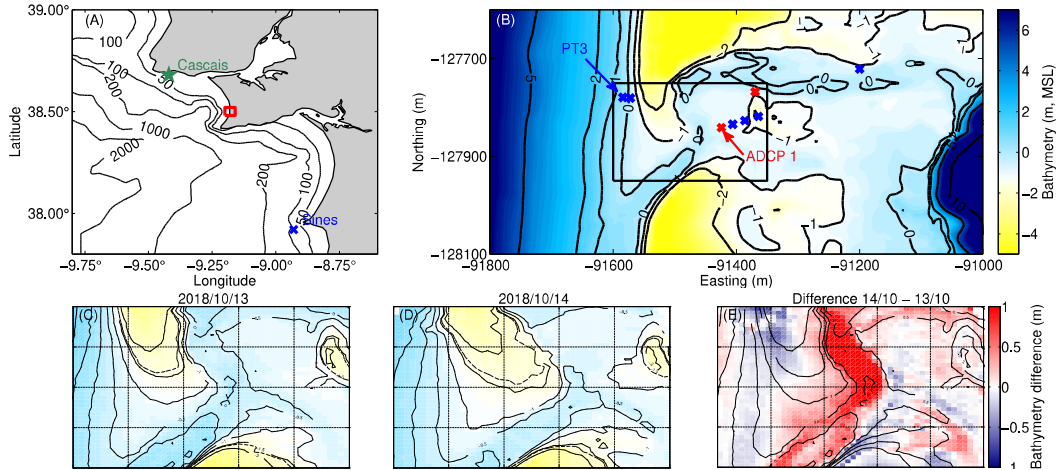
Figure 1. (A) Locations of the study area in Portugal (red box) and the nearest operating wave buoy (blue cross) and tide gauge (green star) during the field campaign. (B) Detailed bathymetry of the study area (m relative to mean sea level, hereafter MSL), showing the location of the ADCPs mounted with OBSs (red crosses) and the pressure transducers (blue crosses). Topo-bathymetry of the inlet region surveyed on the 13/10/2018 (C), the 14/10/2018 (D) and difference between both (E). Coordinates of (B)-(E) are in meters (coordinates are in ETRS89-PTTM06) and the thick dotted line in (C)-(D) corresponds to the maximum sustained water level reached inside the lagoon during the field campaign ($z = -1.6$ m).

2 Field campaign and data analysis

The study area corresponds to the Albufeira Lagoon, a $1.3\,km^2$ lagoon located along the West coast of Portugal and connected to the sea through a shallow, wave-dominated and intermittently closed inlet [*Fortunato et al.*, 2014]. Tides range from 0.55 to 3.86 m seaward of the inlet but are strongly distorted and attenuated inside the lagoon. The offshore annual-mean significant wave height is about 1.9 m but can exceed 10.0 m during storms [*Fortunato et al.*, 2017]. The sediments in the region of the inlet are coarse, with a median grain size d_{50} ranging from 0.55 to 0.75 mm [*Fortunato et al.*, 2014].

A field campaign was carried out in the Albufeira Lagoon Inlet between the 12/10/2018 and the 16/10/2018 under storm waves associated with the ex-tropical hurricane Leslie, which made landfall about 150 km to the North of the study area. According to the nearest operating wave buoy during the campaign (Sines, Fig. 1-A), the offshore spectral significant wave height $H_{m0,G}$ reached a maximum of 5 m and the peak wave period T_p increased from 12 s to 16 s (Fig. 2-B). Six pressure transducers (hereafter PT) continuously measuring at 4 Hz and buried about 0.05 m in the bed were deployed on both sides of the inlet and two high-resolution acoustic Doppler current profilers (hereafter ADCP) were deployed around the flood delta (Fig. 1-B). These two ADCPs were mounted with PTs and optical backstatter sensors (hereafter OBS) measuring at 2 Hz at the location of the first measuring cell (the blanking distance was set to 0.10 m). At ADCP1, the first measuring cell was located 0.25 m from the bed (that is 1.16 m above mean sea-level, hereafter MSL), which implies that currents were not measured about 2 hours before and after low tide in the lagoon.

Due to weather forecasts suggesting that offshore $H_{m0,G}$ could reach 10 m, we expected dramatic morphological changes near the inlet channel during the peak of the storm and so we did not run the risk of deploying instruments in this area. Each sensor was positioned with

a differential GNSS, which provides horizontal and vertical precisions of a few centimeters. This GNSS was also used to survey the intertidal topography of the inlet region at each low tide on a daily basis.

For each sensor, bottom pressure measurements were first corrected for sea level atmospheric pressure measured at the nearby meteorological station of Cascais (Fig. 1-A). The entire record was split into consecutive bursts of 20 minutes and only the bursts in which the sensor was continuously submerged were considered. Bottom pressure energy density spectra $E_p(f)$ were computed using Fast Fourier Transforms, with 10 Hanning-windowed segments, which results in 20 degrees of freedom with a frequency resolution of 0.0046 Hz. These pressure spectra were then converted into elevation spectra $E(f)$ considering linear wave theory. According to a sensitivity analysis, accounting for tidal currents in the dispersion relation has only marginal effects on the correction.The spectral significant wave height H_{m0} was computed as:

$$H_{m0} = 4\sqrt{m_0} \tag{1}$$

with

$$m_0 = \int_{f_{min}}^{f_{max}} E(f)df \tag{2}$$

In the gravity band, (f_{min}, f_{max}) were set to $(0.04, 0.5)$ Hz. A fixed frequency cutoff between short and IG waves was considered because incident wave periods varied little during the field campaign. In the IG band, $H_{m0,IG}$ was integrated between 0.0046 and 0.04 Hz.

The ADCPs were set to measure 10 minute-mean velocity profiles with a 0.1 m vertical resolution followed by 20 minutes of continuous measurements at 2 Hz, where current velocities were averaged over a 0.5 m-thick cell. Depth-integrated current velocities were computed based on velocity profiles while their short-term variability was investigated using 20 minute-long samples at 2 Hz. As the OBSs were synchronized to the ADCPs, they provided data with the same temporal structure. The OBS signal intensity was converted into sediment concentration after a calibration in the laboratory, using sediment samples collected at the location of each ADCP.

3 Results

Digital elevation models (hereafter DEM) with a spatial resolution $\Delta x = 5$ m were derived from the topographic surveys. The comparison between the 13/10/2018 and 14/10/2018 DEMs reveals dramatic morphological changes (Fig. 1-C to E). First, the two sandspits bounding the inlet migrated towards the lagoon by 30 to 50 m. The seaward side of these sandspits suffered substantial erosion, with a lowering of the berm locally reaching 1 m, which corresponds to a local horizontal retreat over 10 m. Second, the main channel suffered a considerable sediment accretion, exceeding 1 m along the northern sandspit. Over the surveyed area (black rectangle on Fig. 1-B), $2800\,\text{m}^3$ of sediment eroded while $10200\,\text{m}^3$ accreted, which results in a clearly positive sediment budget ($7400\,\text{m}^3$). The morphological changes of the inlet after the field campaign were monitored qualitatively until its full closure based on satellite images originating from the Sentinel-2 mission (Appendix A.1). The analysis of available images reveals that morphological changes of the lagoon entrance remained very modest (Fig. A.1), without any clear trend since the large sediment accretion that occurred during the storm Leslie. On the 01/11/2018, the main channel width was of the order of 10 m and apparently very shallow while the lagoon was totally closed on the 09/11/2018.

In order to better understand the causes for these morphological changes, water levels, waves and currents measured during the field campaign were further analyzed. Fig. 2-A
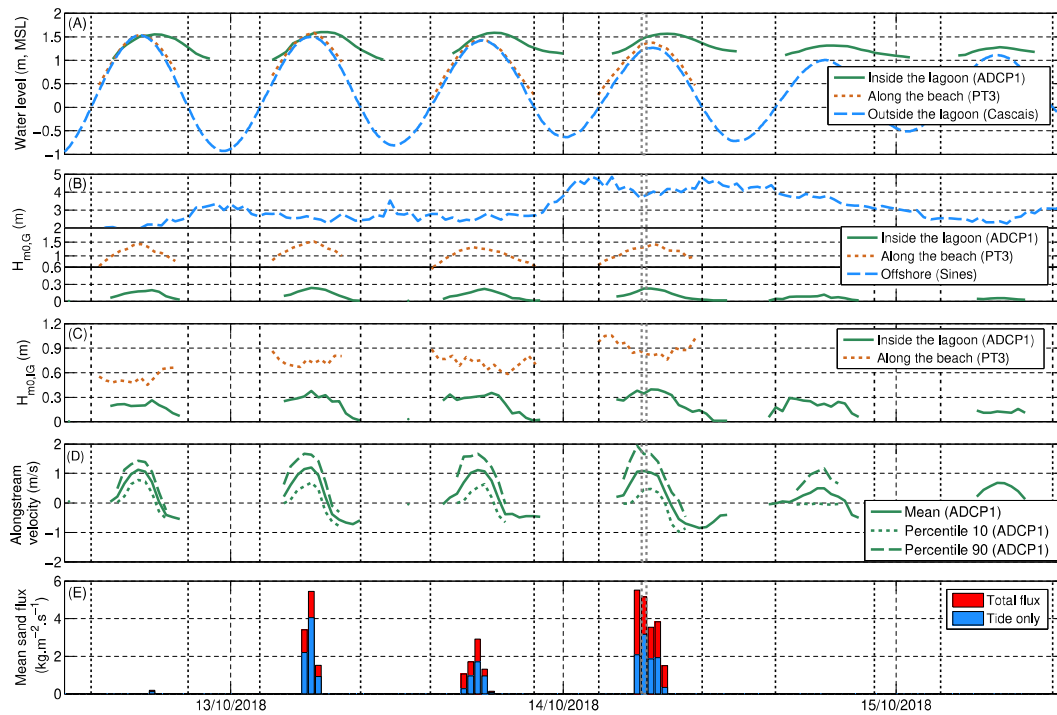
Figure 2. Hydro-sedimentary bulk parameters during the field campaign: (A) Water level variations around mean sea level (m); (B) significant wave height of short waves (m); (C) significant wave height of IG waves (m); (D) mean and percentile 10 and 90 of low-pass filtered alongstream current velocities and (E) mean sand fluxes as observed and owing to tidal currents only. The grey dotted rectangle corresponds to the time of the time-series presented in Fig. 3.

shows water levels measured at the nearby tide gauge of Cascais (Fig. 1-A), along the sandspit outside the lagoon (PT3, Fig. 1-B) and inside the lagoon (ADCP1, Fig. 1-B), all vertically referenced with respect to MSL. The comparison between these data reveals firstly that water levels at PT3 were slightly higher than at Cascais (by up to 0.35 m), which is explained by the development of a wave setup along the coast. Inside the lagoon, water levels were also higher than at Cascais but the tidal range was dramatically reduced, a process already described by *Dodet et al.* [2013]. In details, the ratio between the tidal range inside the lagoon and at Cascais dropped from 0.3 on the 13/10/2018 to 0.15 on the 15/10/2018. Tides inside the lagoon were also strongly distorted, with floods lasting on average $4h00$ and ebbs lasting $8h20$.

In deep water, $H_{m0,G}$ increased from 2 m at the beginning of the campaign to 5 m at the peak of the storm (Fig. 2-B) while the peak wave period T_p increased from 11 s to 16 s (not shown). Along the adjacent beaches, $H_{m0,G}$ was depth-limited and therefore tidally modulated, with maximum values at high tide ranging from 1.3 m to 1.5 m (Fig. 2-B). Note that this sensor was always located in the inner surf zone, so that waves were certainly higher at the breaking point, although we were not able to deploy any sensor there. Inside the lagoon, $H_{m0,G}$ decreased drastically and ranged from about 0.2 m during the first four tidal cycles to 0.1 m or less during the last two tidal cycles. $H_{m0,G}$ increased with the water depth, suggesting that short waves were also depth-limited inside the lagoon. However, the ratio between $H_{m0,G}$ and the local water depth ranges from 0.15 to 0.40, which suggests that depth-limitation was not local but rather occurred over the ebb-delta and the southern part of the northern sandspit. Also, the time series of individual short wave height were positively correlated with water depth fluctuations associated with IG waves (mean $R^2 = 0.47 \pm 0.12$, where $\pm$ corresponds to one standard deviation), which is explained by the fact that short waves were less depth-limited when traveling over the crest of an IG wave. Finally, for a given water level, short waves were substantially higher during flood than ebb, a behaviour that was already observed by *Dodet et al.* [2013] and *Bertin and Olabarrieta* [2016] and explained by wave blocking due to strong opposing ebb currents in shallow depth.

Along the adjacent beaches, $H_{m0,IG}$ increased from 0.6 m at the beginning of the campaign to 1.1 m at the peak of the storm (Fig. 2-C). $H_{m0,IG}$ were slightly tidally modulated, but unlike short waves, they were maximum close to the waterline. Inside the lagoon, $H_{m0,IG}$ increased from 0.2 m during the first tidal cycle to 0.4 m at the peak of the storm. Similar to short waves, IG waves almost disappeared after mid-ebb, which was already observed at this site by *Bertin and Olabarrieta* [2016] and explained by strong opposing currents in shallow depth.

At the location of ADCP1 (Fig. 1-A), 20 minute-mean current velocities reached 1.1 m.s^{-1} during flood and -0.8 m.s^{-1} during ebb for the first four tidal cycles. During the last two tidal cycles, these values dropped to 0.5 m.s^{-1} and -0.5 m.s^{-1}, respectively (Fig. 2-D). The shorter-term variability of alongstream currents was characterized based on the mean current speed U_m and their 10 and 90 percentiles (Fig. 2-D). These percentiles show that, during the first three tidal cycles, maximum current speed values exceeded U_m by 50% about 10% of the time while minimum values were 50% lower than U_m about 10% of the time. Around the peak of the storm, maximum values exceeded U_m by almost 100% about 10% of the time while currents were nearly canceled 10% of the time.

A time-series of instantaneous water levels and alongstream current velocities around the peak of the storm is shown on Figs. 3-A and -B. The low-pass filtered water levels reveal the presence of IG waves of individual height ranging from 0.1 m to 0.5 m. The crests of these IG waves are associated with peaks in alongstream velocities that reach 2.5 m.s^{-1} while the passage of their troughs coincides with periods where flood currents are strongly reduced or even briefly reverted (e.g., see Fig. 3-C around $t = 750$ s). Low-pass filtered water level variations and alongstream velocities are highly correlated, with a correlation coefficient $r = 0.88$ ($p = 0$). Sediment concentrations measured at the bottom of the first ADCP cell also display large fluctuations and range from 0.5 g.l^{-1} to over 40 g.l^{-1}. In details,
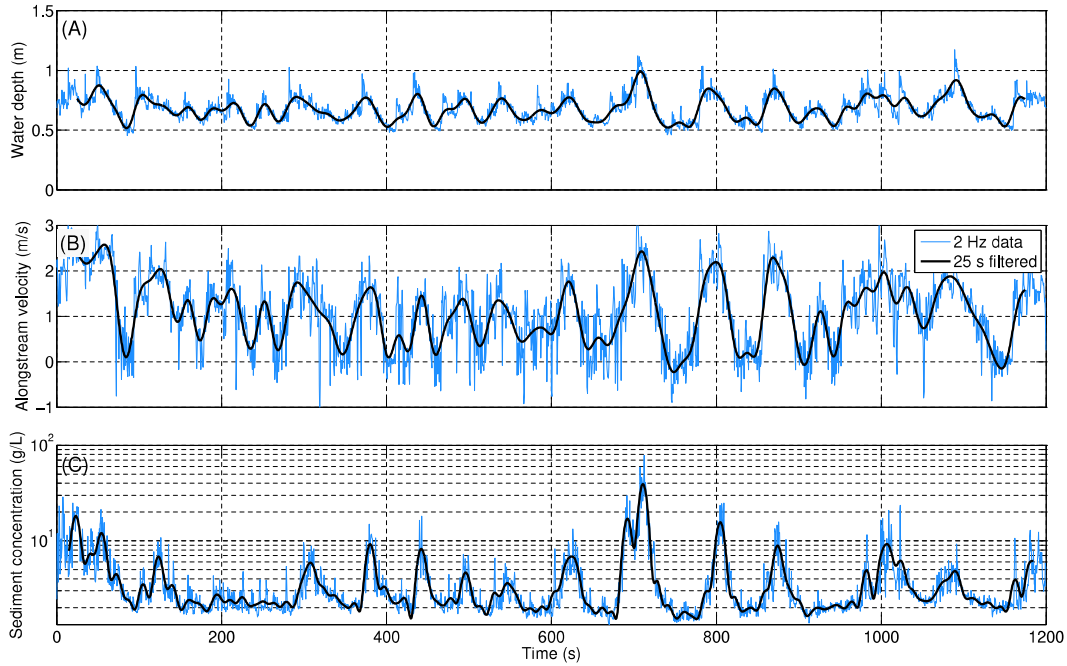
Figure 3. Selected time-series at the ADCP1 starting at 6h00 on the 14/10/2018: (A) Water depth (m); (B) alongstream current velocities and (C) sediment concentration. The blue thin line corresponds to the raw data at $2\,Hz$ and the black thick line to low-pass filtered data with a $0.04\,Hz$ frequency cutoff.

large sediment concentrations systematically match IG wave crests and associated peaks in alongstream currents. Low-pass filtered suspended sediment concentrations (hereafter SSC) and alongstream velocities are also well correlated, with a correlation coefficient $r = 0.61$ ($p = 0$). According to *van Rijn* [2007], the transport of sediment particles in suspension is proportional to $U^{3.4}$, where U is the current velocity, which implies that SSC is proportional to $U^{2.4}$. Considering $U^{2.4}$ instead of U yields higher correlations between alongstream currents and SSC, with a correlation coefficient reaching $r = 0.76$ ($p = 0$). In order to quantify the contribution of the velocity peaks driven by IG waves to suspended sediment transport, we compared suspension sand fluxes as observed and suspension sand fluxes that would be driven by tidal currents only (i.e. using U_m), assuming a $U^{3.4}$ dependency (Fig. 2-E). This analysis confirms that peaks in current velocity driven by IG waves strongly enhance suspensed sand fluxes compared to a situation with tidal currents only, from 35% to 63% during the first two tidal cycles to more than 400% around the storm peak (210% on average over the field campaign), when IG waves were the largest. The contribution of short waves to suspended sediment transport was also evaluated, considering the transport formula of *van Rijn* [2007] fed with low-pass filtered time series of water levels, current velocities and individual short wave heights. The comparison between a situation with and without short waves suggests that short waves increase suspended sand transport by 21% ($26 \pm 7\%$ on average over the field campaign). Such a modest contribution is related to the strong decrease of short waves inside the lagoon, with $H_{m0,G}$ ranging from 0.06 to $0.24\,m$ at ADCP1 over the field campaign.

4 Discussion and conclusions

Bertin et al. [2009] showed that the dynamics of such shallow inlets was controlled by the balance between tidal asymmetry, which promotes inlet enlargement, and wave-driven

processes, which promote sediment accretion at the lagoon entrance. *Bertin and Olabarrieta* [2016] suggested that IG waves could also have a key contribution to inlet dynamics and closure. The present dataset provides a unique opportunity to verify this hypothesis.

The analysis of water levels and current velocities measured at the Albufeira Lagoon showed that the passage of IG waves was associated with peaks in current velocities, temporarily exceeding $2.5\,\mathrm{m.s^{-1}}$. These peaks increased instantaneous sand fluxes by up to two orders of magnitude. Once integrated over 20 minute-long samples, measured sand fluxes were estimated to be on average 200% larger than in a situation without IG waves, and as much as 400% when IG waves were largest. This phenomenon only occurs during flood, because IG waves were blocked during most of the ebb by opposing currents. We propose that, once integrated over a tidal cycle, this process directly explains the considerable sediment accretion that took place at the entrance of the lagoon during the ex-tropical hurricane Leslie. Note that, due to the low elevation of the northern sandspit, a large part of its surface-area was continuously submerged and exposed to flood currents around high tide (Fig. 1-C). Therefore, the mechanism described above was certainly not limited to the inlet main channel but was probably active over the sandspit area located below high tide water level, that is $z = -1.6\,\mathrm{m}$. Additionally, both visual field observations and repetitive topographic surveys revealed that the northern sandspit suffered morphological changes up to $z = -2.5\,\mathrm{m}$. Considering *Stockdon et al.* [2006] using a mean surf zone slope $\beta = 0.05$ and deep water wave conditions as measured in Sines (Fig. 1-A), the runup 2% exceedence $R_{2\%}$ would be of the order of $1.4\,\mathrm{m}$, which yields a maximum runup level around $3.0\,\mathrm{m}$ above MSL. Therefore, overwashes driven by IG waves could explain the large sediment deposition observed inside the lagoon along northernmost part of the North spit (Fig. 1-E).

The topographic surveys carried out after the peak of the storm (not shown) as well as the time series of Sentinel-2 images (A.1) suggest that the lagoon entrance displayed very limited morphological changes during the two weeks that followed the storm. Water levels (Fig. 2-A) and current velocities (Fig. 2-D) measured inside the lagoon revealed that the tidal range and currents decreased by a factor of two after the passage of Leslie. This combination of topographic and hydrodynamic measurements suggests that the large sediment accretion at the entrance of the lagoon damped tidal propagation inside the lagoon, so that the inlet became almost inactive during the two weeks following Leslie, until the main channel fully closed. We propose that the final closure of the inlet channel could result from the combination of longshore transport and swash processes [e.g. *Baldock et al.,* 2008], which promoted the development of the steep berm that is usually present along the beachface.

In conclusion, this study demonstrates that the propagation of IG waves in a shallow tidal inlet can have a fundamental contribution to its hydro-sedimentary dynamics and largely contributed to its closure. Although based on a single case study, this unreported mechanism is likely to be valid for most shallow inlets exposed to the open ocean, since IG waves develop as soon as groups are present in the incident short waves reaching the coast. Global IG wave climate computed by *Ardhuin et al.* [2014] would suggest that IG waves should be particularly relevant for the dynamics of shallow inlets located in northwestern and southwestern America, western Europe, northwestern and southwestern Africa and western and southern Australia. The relevance of IG waves will also have to be verified at other types of inlets, including larger and deeper systems, for which the impact of IG waves is totally unknown according to our knowledge. Up to now, IG waves were usually not represented in numerical models when applied to tidal inlets: this study suggests that including IG waves in future modelling studies should improve model predictive skills, and possibly allow to reproduce for the first time tidal inlet closure without unrealistic parameterizations. The contribution of swash processes to the final closure of inlet channels will also have to be analyzed in the future.

Acknowledgments

## References

Anthony, E., L. Oyédé, and J. Lang (2002), Sedimentation in a fluvially infilling, barrier-bound estuary on a wave-dominated, microtidal coast: The Ouémé River Estuary, Benin, West Africa, *Sedimentology*, *49*(5), 1095–1112, doi:10.1046/j.1365-3091.2002.00491.x.

Ardhuin, F., A. Rawat, and J. Aucan (2014), A numerical model for free infragravity waves: Definition and validation at regional and global scales, *Ocean Modelling*, *77*, 20–32.

Baldock, T., F. Weir, and M. Hughes (2008), Morphodynamic evolution of a coastal lagoon entrance during swash overwash, *Geomorphology*, *95*(3), 398–411, doi: https://doi.org/10.1016/j.geomorph.2007.07.001.

Bertin, X., and M. Olabarrieta (2016), Relevance of infragravity waves at a wave-dominated inlet, *Journal of Geophysical Research*, (212), 5418–5435, doi:10.1002/2015JC011444.

Bertin, X., A. B. Fortunato, and A. Oliveira (2009), A modeling-based analysis of processes driving wave-dominated inlets, *Continental Shelf Research*, *29*(5-6), 819–834, doi: 10.1016/j.csr.2008.12.019.

Bertin, X., A. de Bakker, A. van Dongeren, G. Coco, G. André, F. Ardhuin, P. Bonneton, F. Bouchette, B. Castelle, W. Crawford, M. Davidson, M. Deen, G. Dodet, T. Guérin, K. Inch, F. Leckler, R. McCall, H. Muller, M. Olabarrieta, D. Roelvink, G. Ruessink, D. Sous, E. Stutzmann, and M. Tissier (2018), Infragravity waves: From driving mechanisms to impacts, *Earth-Science Reviews*, *177*, 774–799.

Cooper, J. (2001), Geomorphological variability among microtidal estuaries from the wave-dominated south african coast, *Geomorphology*, *40*(1-2), 99–122, doi:10.1016/S0169-555X(01)00039-3.

Dodet, G., X. Bertin, N. Bruneau, A. B. Fortunato, A. Nahon, and A. Roland (2013), Wave-current interactions in a wave-dominated tidal inlet, *Journal of Geophysical Research: Oceans*, *118*(3), 1587–1605, doi:10.1002/jgrc.20146.

Drusch, M., U. Del Bello, S. Carlier, O. Colin, V. Fernandez, F. Gascon, B. Hoersch, C. Isola, P. Laberinti, P. Martimort, A. Meygret, F. Spoto, O. Sy, F. Marchese, and P. Bargellini (2012), Sentinel-2: ESA's optical high-resolution mission for GMES operational services, *Remote Sensing of Environment*, *120*, 25–36, doi:10.1016/j.rse.2011.11.026.

Duong, T., R. Ranasinghe, D. Walstra, and D. Roelvink (2016), Assessing climate change impacts on the stability of small tidal inlet systems: why and how?, *Earth-Science Reviews*, *154*, 369–380.

Fortunato, A., P. Freire, X. Bertin, M. Rodrigues, J. Ferreira, and M. Liberato (2017), A numerical study of the february 15, 1941 storm in the tagus estuary, *Continental Shelf Research*, *144*, 50–64.

330 Fortunato, A. B., A. Nahon, G. Dodet, R. A. Pires, C. M. Freitas, N. Bruneau, A. Azevedo,
331   X. Bertin, P. Benevides, C. Andrade, and A. Oliveira (2014), Morphological evolution of
332   an ephemeral tidal inlet from opening to closure: the Albufeira Inlet, Portugal, *Conti-*
333   *nental Shelf Research*, *73*, 49–63.

334 González-Villanueva, R., M. Pérez-Arlucea, and S. Costas (2017), Lagoon water-level oscil-
335   lations driven by rainfall and wave climate, *Coastal Engineering*, *130*, 34–45.

336 Hanes, D., K. Ward, and L. Erikson (2011), Waves and tides responsible for the intermit-
337   tent closure of the entrance of a small, sheltered tidal wetland at San Francisco, CA,
338   *Continental Shelf Research*, *31*(16), 1682–1687.

339 McSweeney, S., D. Kennedy, I. Rutherfurd, and J. Stout (2017), Intermittently closed/open
340   lakes and lagoons: Their global distribution and boundary conditions, *Geomorphology*,
341   *292*, 142–152, doi:https://doi.org/10.1016/j.geomorph.2017.04.022.

342 Moreno, I., A. Ávila, and M. Losada (2010), Morphodynamics of intermittent coastal lagoons
343   in Southern Spain: Zahara de los Atunes, *Geomorphology*, *121*(3-4), 305–316.

344 Orescanin, M., and J. Scooler (2018), Observations of episodic breaching and closure at an
345   ephemeral river, *Continental Shelf Research*, *166*, 77–82.

346 Ranasinghe, R., and C. Pattiaratchi (2003), The seasonal closure of tidal inlets: Causes and
347   effects, *Coastal Engineering Journal*, *45*(4), 601–627, doi:10.1142/S0578563403000919.

348 Stockdon, H. F., R. A. Holman, P. A. Howd, and A. H. Sallenger Jr (2006), Empirical
349   parameterization of setup, swash and runup, *Coastal Engineering*, *53*, 573–588.

350 van Rijn, L. (2007), Unified view of sediment transport by currents and waves. ii: Suspended
351   transport, *Journal of Hydraulic Engineering*, *133*(6), 668–689, doi:10.1061/(ASCE)0733-
352   9429(2007)133:6(668).

353 Williams, M. E., and M. T. Stacey (2016), Tidally discontinuous ocean forcing in bar-built
354   estuaries: The interaction of tides, infragravity motions, and frictional control, *Journal*
355   *of Geophysical Research*, *121*, 571–585, doi:10.1002/2015JC011166.

A: Morphological evolution of the inlet based on Sentinel images

The morphological changes of the Albufeira Lagoon Inlet outside the field campaign were qualitatively monitored based on satellite images obtained from the Sentinel-2 mission. Sentinel-2 is a large swath, high-resolution, multi-spectral satellite mission launched by the European Space Agency in June 2015 (Sentinel-2A) and complemented with a second satellite launched in March 2017 (Sentinel-2B, *Drusch et al.* [2012]). These two satellites are flying along the same orbit but out of phase and allow for a minimum revolution period of about 6 days. In the visible domain, the spatial resolution is 10 m.
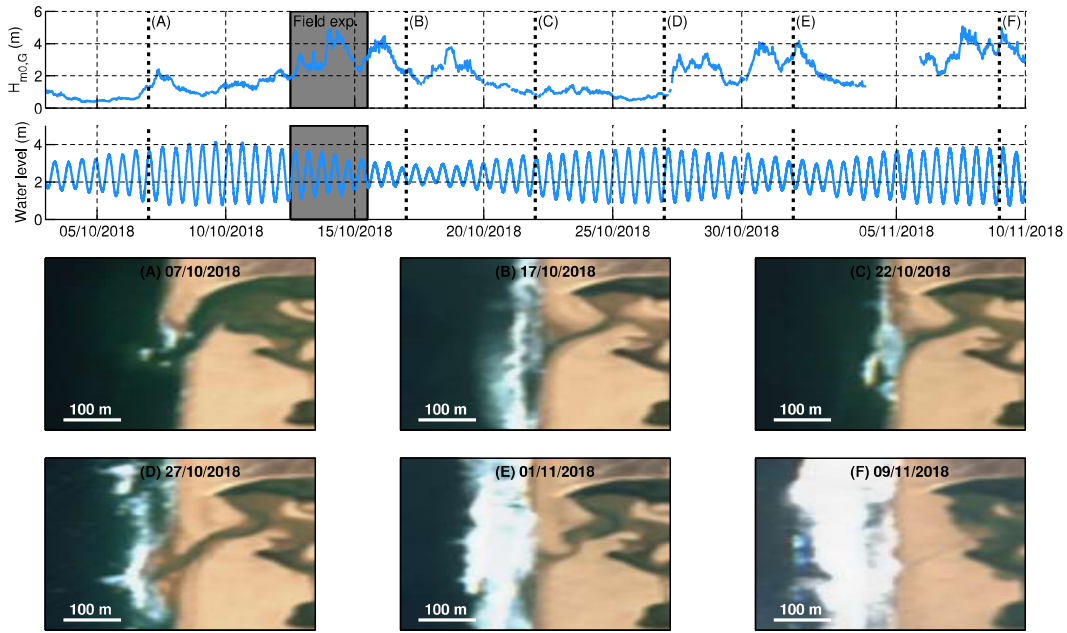
Figure A.1. Time series of significant wave height at Sines Buoy and water levels at Cascais tide gauge (Fig. 1-(A)), where the vertical dashed-dotted black lines correspond to the dates of selected Sentinel images (A) to (F), showing that considerable morphological changes took place during the field campaign, after which the inlet remained poorly dynamic until full closure.